

# Detailed assessment of low-voltage zones localization by cardiac MRI in patients with implantable devices

**Running Title: Optimization strategies for scar localization using CMR in patients with ICDs**

Michele Orini PhD\* <sup>1,2</sup>, Andreas Seraphim MBBS\* <sup>1,3</sup>, Adam Graham PhD <sup>2</sup>, Anish Bhuva PhD<sup>1,3</sup>, Ernesto Zacur PhD <sup>4</sup>, Peter Kellman PhD<sup>5</sup>, Richard Schilling MD MRCP FHRs <sup>2</sup>, Ross Hunter PhD, MRCP FHRs<sup>2</sup>, Mehul Dhinoja MRCP FHRs <sup>2</sup>, Malcolm C. Finlay PhD<sup>2</sup>, Syed Ahsan MD FRCP <sup>2</sup>, Anthony W. Chow MD MRCP FHRs <sup>2</sup>, James C. Moon MD <sup>1,3</sup>, Pier D. Lambiase PhD FRCP FHRs<sup># 1,2</sup>, Charlotte Manisty PhD<sup># 1,3</sup>

\* Joint first authors, # Joint senior Authors

1: Institute of Cardiovascular Science, University College London, UK

2: Department of Cardiac Electrophysiology, Barts Heart Centre, Barts Health NHS Trust, London, United Kingdom

3: Department of Cardiovascular Imaging, Barts Heart Centre, Barts Health NHS Trust, London, United Kingdom

4: Department of Biomedical Engineering, University of Oxford, Oxford, UK.

5: National Institutes of Health, Bethesda, USA

## Corresponding authors:

- Prof Pier D. Lambiase, Institute of Cardiovascular Science, 5 University St, London WC1E 6JF, Email: [p.lambiase@ucl.ac.uk](mailto:p.lambiase@ucl.ac.uk), +44(0)203 679 4407
- Dr Charlotte H. Manisty, Department of Cardiac Imaging, Barts Heart Centre, W Smithfield, London EC1A 7BE. Email: [c.manisty@ucl.ac.uk](mailto:c.manisty@ucl.ac.uk)

## Sources of Funding

AB and AS are supported by doctoral research fellowships from the British Heart Foundation (FS/16/46/32187 and FS/18/83/34025). JCM, PDL, MO and CM are directly and indirectly supported by the University College London Hospitals and

- 7 Barts Hosptial NIHR Biomedical Research Centres. PL has received research grants
- 8 from Boston Scientific, Medtronic and Abbott and speaker fees from Medtronic.

## Abstract

*Aims:* Scar evaluation by late gadolinium enhancement cardiac magnetic resonance (LGE-CMR) can assist ventricular tachycardia (VT) ablation, but challenges with electro-anatomical maps (EAMs) co-registration and presence of imaging artefact from cardiac implantable electronic devices (CIED) limit accuracy. We assessed the performance and limitations of low-voltage zones (LVZ) localization by optimised LGE-CMR scar imaging in patients with CIEDs.

*Methods:* 10 patients underwent VT ablation and pre-procedural LGE-CMR using wideband imaging. Scar was segmented from CMR pixel signal intensity (PSI) maps using commercial software (ADAS) with bespoke tools and compared to detailed EAMs (CARTO). Co-registration of EP and imaging derived scar was performed using the aorta as a fiducial marker and the impact of co-registration was determined by assessing intra/inter-observer variability and using computer simulations. Spatial smoothing was applied to assess correlation at different spatial resolutions and to reduce noise.

*Results:* PSI maps localized low-voltage zones ( $V < 1.5$  mV) with area under the ROC curve  $AUC = 0.82$  ( $0.76$ – $0.83$ ), sensitivity =  $74\%$  ( $71\%$ – $77\%$ ) and specificity =  $78\%$  ( $73\%$ – $83\%$ ) and correlated with bipolar voltage,  $r = -0.57$  ( $-0.68$  –  $-0.42$ ) across patients. In simulations, small random shifts and rotations worsened LVZ localization in at least some cases. The use of the full aortic geometry ensured high reproducibility of LVZ localization ( $r > 0.86$  for AUC). Spatial smoothing improved localization of LVZ. Results for LVZ with  $V < 0.5$  mV were similar.

*Conclusion:* In patients with CIEDs, novel wideband CMR sequences and personalised co-registration strategies can localize LVZ with good accuracy and may assist VT ablation procedures.

**Keywords:** Cardiac mapping, Cardiovascular MRI, Scar, Ventricular tachycardia, Ablations

## Condensed Abstract

Cardiac magnetic resonance (CMR) imaging has the potential to localize scar non-invasively and improve ventricular tachycardia (VT) ablation. However, artefacts due to implantable devices (CIEDs), inaccuracy in co-registration with electro-anatomical maps and noise may limit its use. We used optimized wideband sequences and image analysis to assess performance and limitations of low-voltage zones (LVZ) localization by CMR in patients with CIEDs. We found that using the thoracic aorta for co-registration provides good point-by-point correlation ( $r \sim -0.60$ ) and good LVZ discrimination ( $AUC \sim 0.80$ ), with high intra- and inter-observer reproducibility. Spatial smoothing improved overall CMR-EAM agreement at the expense of reducing spatial resolution.

## Abbreviations

VT: Ventricular Tachycardia

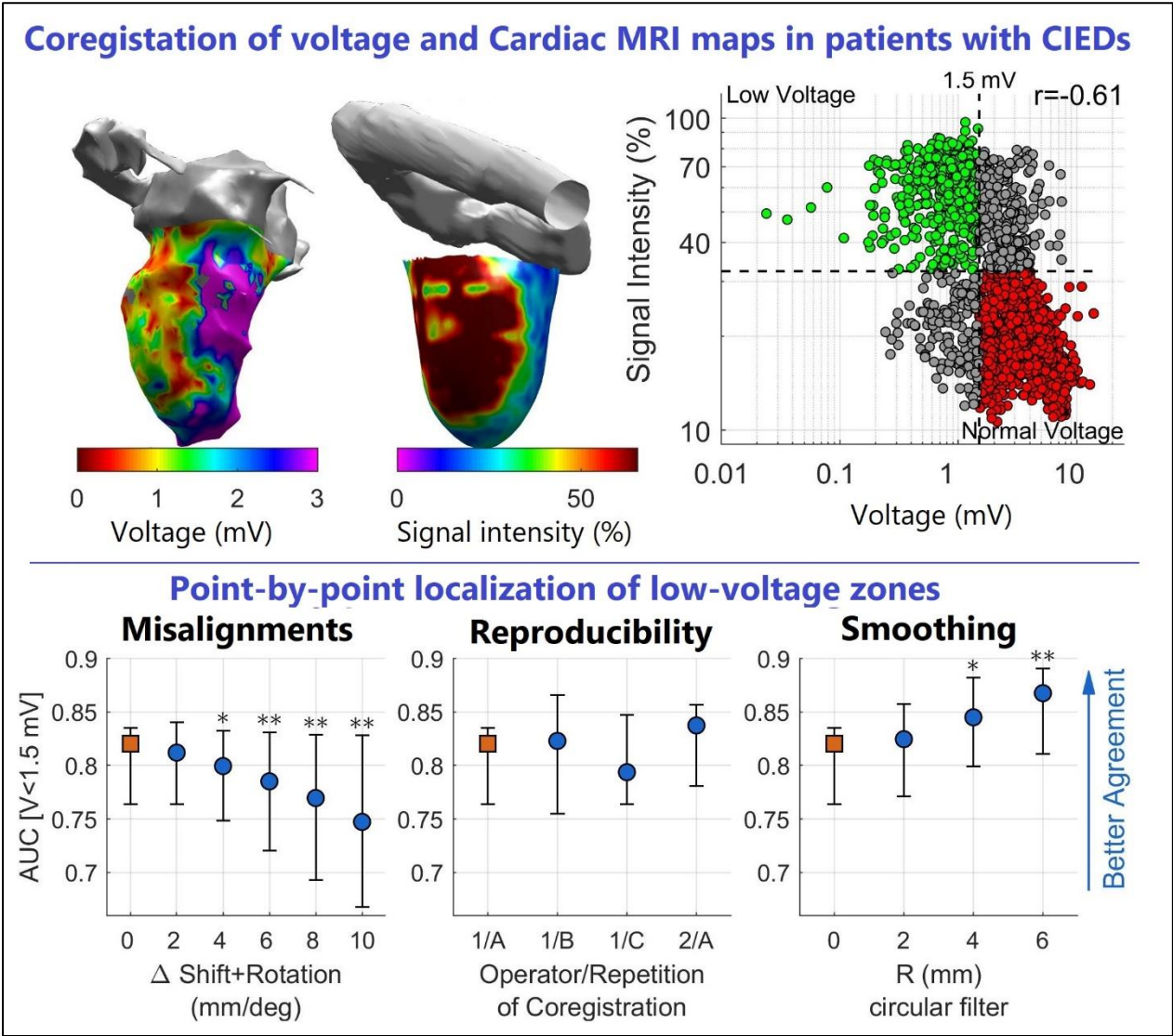
EAM: Electro-anatomical mapping

LGE-CMR: Late Gadolinium enhanced Cardiac Magnetic Resonance

CIED: Cardiac Implantable Electronic Device

LVZ: Low-voltage Zone

PSI: Pixel Signal Intensity



## 26    **Introduction**

27    Catheter ablation improves outcomes in patients with frequent life-threatening  
28    ventricular tachycardia (VT). However, VT recurrence rates remain unacceptably  
29    high necessitating the pursuit of more effective ablation strategies (1). Late  
30    gadolinium enhancement cardiac magnetic resonance (LGE-CMR) can provide non-  
31    invasive visualisation of arrhythmogenic substrate (2–6) and its integration with  
32    electro-anatomical mapping (EAM) can improve procedural outcomes (7–9). Indeed,  
33    recent work has proposed the utilisation of an MRI-guided approach (9), based on  
34    EAM system and CMR-derived scar co-registration. The integration of LGE-CMR  
35    scar maps and EAM for VT ablation is however not widespread. There are several  
36    reasons for this. Firstly, the precise co-registration of whole heart LGE-CMR with  
37    EAM is challenging. Secondly, most patients requiring VT ablation have cardiac  
38    implantable electronic devices (CIEDs) in-situ. Although scanning can now be  
39    performed safely with appropriate protocols (10,11), meaning almost all patients  
40    could now have LGE-CMR, the CIED itself generates image artefact (signal dropout,  
41    hyperintensity artefact) that hinders scar delineation. Dedicated sequences  
42    incorporating a wideband inversion pulse can reduce this (10), but few studies have  
43    examined feasibility of LGE-CMR and EAM co-registration in these patients (8,12,13)  
44    and the agreement in scar localization between the two modalities remains  
45    undetermined. In this study, we deploy a novel wideband LGE sequence that is fast,  
46    free-breathing and incorporates phase-sensitive inversion recovery (10). We  
47    investigate the spatial correlation between low-voltage zones from state of the art  
48    EAM and 3D CMR pixel signal intensity (PSI) maps in patients with CIEDs (10) and  
49    focused on optimal approaches for co-registration that maximise clinical utility.

## 50    **Methods**

### 51    **Study population**

52    The study was approved by the National Health Service Research Ethics Committee  
53    (14/LO/0360) and Health Research Authority (HRA) and was conducted in  
54    accordance with the Declaration of Helsinki. All subjects provided written, informed  
55    consent. Ten (n=10) consecutive patients (1 female, median age 75 years,  
56    interquartile range 70 – 79 years, 9 ischemic cardiomyopathy, 1 non-ischaemic  
57    dilated cardiomyopathy) with CIEDs (5 ICD, 5 CRT-D, 50% non-MR conditional)  
58    undergoing catheter VT ablation between 2017 and 2019 (8 first time, 2 repeat  
59    ablations, Table 1) were included in the analysis. Specifically, patients were included  
60    if they underwent LGE-CMR shortly before catheter ablation and if a detailed LV  
61    substrate map and a complete aortic geometry, including ascending, arch and  
62    descending aorta, were collected during the electrophysiological study. In all  
63    patients, catheter ablation was performed because of recurrent VTs and frequent  
64    ICD therapy. Five cases were elective and 5 were urgent cases for treatment of  
65    incessant VT or VT storm. Among the 9 patients with ischaemic cardiomyopathy,  
66    myocardial infarction was more frequently seen in the anterior wall (bullseye plot of  
67    scar distribution is shown in the Supplementary Material, Figure S1).

### 68    **CMR protocol and data analysis**

69    All patients underwent LGE-CMR prior to their procedure. CMR studies were  
70    performed on a 1.5T scanner (Aera, Siemens Healthineers, Erlangen, Germany)  
71    using a 30-channel phased array receiver coil, scanned at Normal Operating Mode  
72    (SAR limit <2 W/kg). In brief, device interrogation and re-programming occurred  
73    immediately before and after scanning, according to international guidelines.



74 Patients were monitored throughout using ECG and pulse oximetry waveform  
75 assessment.

76 An axial stack of images through the thorax was acquired for visualisation of  
77 extracardiac structures, including the thoracic ascending and descending aorta to  
78 enable co-registration with EAM data. This used a black blood Half-Fourier  
79 Acquisition Single-shot Turbo spin Echo (HASTE) sequence, with 5mm slice  
80 thickness and zero gap between slices. Late gadolinium images were acquired 10-  
81 15 min after administration of 0.1 mmol/kg of Dotarem (Guerbet S.A.,Paris). The  
82 sequence used was a 2D motion-corrected (free-breathing) single-shot FLASH  
83 sequence with a 3.9 kHz (wideband) inversion pulse, with flip angle of 10°, phase  
84 sensitive inversion recovery (PSIR)(10) and 24 averages to recover signal to noise.  
85 Contiguous 4 mm short-axis slices were acquired with spatial resolution of 1.9x1.4  
86 mm, which was interpolated to 1.4x1.4 mm for display and analysis. Epicardial and  
87 endocardial borders were segmented, generating a 3D pixel signal intensity map of  
88 the left ventricle (LV) using custom software (ADAS-VT, Galgo Medical, Spain) (6–8)  
89 . Nine concentric surface layers from sub-endocardium (10% of wall thickness) to  
90 sub-epicardium (90% of wall thickness) were created automatically. Subsequently,  
91 pixel signal intensity (PSI) maps were projected over each LV layer using a trilinear  
92 interpolation and color-coding to visualize PSI distribution. PSI was normalized, with  
93 global minimum and maximum across all layers set equal to 0 and 100, respectively.  
94 A tool in the same software was also used to create a 3D surface representation of  
95 the aorta from the 2D axial anatomical images and to co-register this with the LV PSI  
96 map.

## EAM protocol and data analysis

Procedures were performed under conscious sedation using diamorphine and midazolam, or general anaesthetic. Vascular access was obtained under ultrasound guidance using Seldinger technique via the right femoral vein and/or right femoral artery. The LV was accessed retrogradely via the aorta in all cases. Trans-septal puncture was additionally performed in 4 cases to gain better overall access and mapping coverage of the LV. A full geometry of the ascending, arch, and descending aorta was created for co-registration with CMR-LGE scar meshes. Collection of this geometry took less than 5 minutes in each case. A voltage map was created using a multipolar catheter (Pentaray, CARTO, Biosense-Webster, CA), and the ST SF Thermocool ablation catheter was also used in some cases. Most of intracardiac mapping was performed continuously with criteria for collecting data including close tissue proximity (using Tissue Proximity Indicator for Pentaray), position stability and contact force within 2-40 g (when using the ablation catheter). Occasionally, data collection was performed manually. EAM generated using less than 100 electrode points were excluded.

CARTO generated meshes describing the spatial distribution of bipolar voltage of the LV endocardium were exported for off-line analysis. Bipolar voltage  $<1.5$  mV and  $<0.5$  mV was considered indicative of scar and dense scar, respectively.

## EAM-CMR comparison

PSI color-coded maps were not visible to operators during the electrophysiological study to reduce potential biases and co-registration of EAM and CMR geometries was performed retrospectively (after each case) using bespoke software (Matlab, The Mathworks, Inc, MA) (14,15) that allows the operator to move and rotate EAM and CMR geometries and inspect the alignment under any viewpoint ([Video 1](#) in

Supplementary Material). Co-registration was manually performed and visually determined by an expert independent of subsequent analysis and blinded to color-coded maps of voltage and PSI (i.e. solely based on anatomical information). Emphasis was placed on the simultaneous alignment of the ascending, arch and descending aorta, and the LV apex. No other extra-cardiac structure was systematically utilised. After co-registration, each vertex belonging to the EAM geometry (i.e. the triangular mesh produced during cardiac mapping) was paired to the closest vertex of the PSI map, provided that the Euclidean distance ( $D$ ) between them was  $D \leq 8$  mm.

The impact of EAM-CMR co-registration on the localization of low-voltage zones was assessed by reproducibility analysis and simulations. Intra- and inter-observer reproducibility was assessed by repeating co-registration twice (same operator, with more than 48 hours between repetitions) and by a second expert operator, respectively. Repeated co-registrations were compared by measuring the difference between the location of the aligned geometries as shifts and rotations (Euler's rule) along and about the XYZ axes. The simulation study was carried out as follows. After co-registration, small shifts and rotations were algorithmically applied to the EAM and low-voltage zones localization re-assessed. In total, the analysis was repeated 320 times per case, consistent with configurations obtained by applying simultaneous shifts and rotations of  $\pm\Delta X$  mm and  $\pm\Delta X^\circ$  along and around the 3 major axes ( $2^6=64$  configurations), where  $\Delta X = 2^\circ, 4^\circ, 6^\circ, 8^\circ$  and  $10^\circ$ . [Video 3](#) in Supplementary Material shows the effect of shifts and rotations of up to  $\pm 10$  mm and  $\pm 10^\circ$  on one representative EAM.

As the agreement between voltage and PSI is thought to be affected by each modality's spatial resolution and noise, we sought to modulate spatial resolution and

reduce noise by implementing spatial smoothing. This assigns to each point in a map the average value of its neighbouring points within a given radius. Systematic variation of this radius (circular linear filters with radius equal to 2, 4 and 6 mm) allowed evaluation of the impact of spatial resolution/noise reduction on agreement between EAM voltage and PSI. [Video 2](#) in Supplementary Material shows the effect of increasing spatial smoothing on representative voltage and PSI maps.

### Statistical analysis

Data distribution is reported as median, 1<sup>st</sup> – 3<sup>rd</sup> quartile. Correlation was assessed using the Spearman's correlation coefficient (r). Assessment of binary classification of low-voltage zones characterized by  $V < 0.5$  mV or  $V < 1.5$  mV was performed using ROC curves. The area under the ROC curve (AUC) as well as sensitivity and specificity obtained using the optimum PSI threshold (threshold corresponding to the point closest to 100 sensitivity and specificity) were estimated for each case. Sensitivity and specificity were then assessed using a fixed PSI threshold equal to the median value of case-specific PSI thresholds. EAM for which the prevalence of low-voltage zones was  $< 3\%$  were not considered. Reported results represent averaged values across CMR layers spanning from sub-endocardium (layer 10%) to mid-myocardium (layer 50%) included. Results for each layer are reported in Supplementary Material.

## Results

CMR scans were performed without complication in all subjects, with no significant changes in device parameters (battery voltage or lead sensitivities, thresholds or impedances) between pre- and post-CMR device interrogations. PSI scar maps were free from artefact in 3 out of the 10 patients. In the 7 remaining patients, artefacts

were most frequently located at the apical cap (n=4) and on the anterior wall (n=3) (Fig. S1 in Supplementary Material). The proportion of LV surface affected by artefacts was 9.7% (1.4% – 13.9%) across patients. The median interval between CMR and electrophysiological study was 2 (5 – 23) days, with no relevant clinical events between procedures in any patient (Table 1).

Meshes of EAMs were derived from 611 (385 – 1,581) electrode points and were composed of 7,859 (6,880 – 14,952) vertices, of which 59% (48% – 65%) were paired to CMR points (Table 2), with the remaining ones often belonging to non-ventricular structures, or the valve plane or being proximal to CMR artefacts. Pooling data from all cases, the distance between CMR and EAM points was 3.36 (1.64 – 5.28) mm. Of all EAM points, 87% and 13% were collected using a Pentaray and a standard ablation catheter, respectively. In 3 cases, intracardiac electrograms were mainly collected with the ablation catheter. In two of these, all points in the EAM meshes had contact force >2 g. In the remaining case, 27% of points in the EAM mesh had either undetermined force or force < 2 g.

On CMR, end diastolic and systolic volumes were 248 (197 – 290) mL and 187 (141 – 227) mL, respectively. There was a good agreement between the area of the LV (excluding the valve plane) measured from EAM and CMR geometries, with correlation coefficient equal to  $r=0.879$  (Supplementary Figure S8). The LV area from EAM was 0.3% (-3.5% – 7.3%) larger than LV area from CMR.

## Correlation between EAM voltage and PSI

Comparison between EAM and PSI maps for 2 representative patients, including point-by-point correlations and case-specific ROC curves, is shown in Figure 1 and Figure S2 in Supplementary Material.

A significant negative correlation between bipolar voltage and PSI was registered in all patients across all cardiac sites, with a correlation coefficient equal to -0.57 (-0.68, -0.42). PSI correlation with unipolar voltage was also significant, but lower, with correlation coefficient equal to -0.49 (-0.65, -0.36). Correlation between endocardial bipolar voltage and PSI and between endocardial unipolar voltage and PSI was not significantly different across different transmural layers, from endocardial to epicardial PSI layers (Fig. S3 in Supplementary Materials).

## Agreement in LVZ localization

Case by case ROC analyses showed good localization of low-voltage zones (Table 2), with AUC for the localization of areas with  $V < 1.5$  mV of 0.82 (0.76 – 0.83), sensitivity of 74% (71% – 77%) and specificity of 78% (73% – 83%). Localization of areas with  $V < 0.5$  mV was similar (Table 2). The correlation coefficient between the area of low-voltage zones from EAM and PSI maps was 0.87 for  $V < 0.5$  mV and 0.79 for  $V < 1.5$  mV (Figure 2). Agreement between CMR and EAM for localization of LVZ was similar in cases where the majority of data was collected using an ablation catheter (n=3) and where a Pentaray (n=7) catheter was used (Supplementary Table S1).

These results were obtained using case-specific ROC-derived PSI thresholds. Similar results were obtained when using a fixed PSI threshold for all cases, taken as the median value of the case-specific PSI thresholds (i.e.  $PSI > 41\%$  for  $V < 1.5$  mV

and PSI>46% for  $V<0.5$  mV, Table 2). Sensitivity and specificity were 71% (65%-81%) and 76% (69%-86%) for  $V<1.5$  mV, and 79% (62%-86%) 67% (67%-77%) for  $V<0.5$  mV, respectively.

As expected, given that voltage maps were collected on the endocardium, low-voltage zones localization was more accurate using endocardial than epicardial PSI layers (Fig. S4 in Supplementary Material). However, accuracy in low-voltage zones localization using PSI was not significantly different for the sub-endocardial as compared to mid-myocardial layer (Supplementary Fig. S4).

Across all patients, mean PSI at ablation sites was 65% (63% – 73%), and 93% (83% – 100%) of ablation sites were located in areas of scar (i.e. above PSI threshold) in PSI maps. The distribution of ablation sites mapped onto a co-registered PSI map, including electrograms recorded at a cardiac site where ablation terminated a subsequently induced VT, is shown for one case in Fig. 4.

Choosing a different minimum distance required for pairing CMR and EAM points modified the number of paired sites without significantly affecting the results (Fig. S7 in Supplementary Material). Finally, rescaling PSI values to their 5<sup>th</sup> and 95<sup>th</sup> percentile value instead of between minimum and maximum did not affect the results (Table 2 in Supplementary Material).

### Effect of co-registration misalignments

Results of the simulation study to assess low-voltage zones localization after algorithmically altering co-registration showed that misalignments can have a strong impact on the agreement between PSI and voltage, with both PSI-voltage correlation and discrimination of low-voltage zones decreasing for increasing shifts/rotations (Figure 3A). Nevertheless, intra- and inter-operator co-registration variability had little

impact on low-voltage zones localization (Figure 3B). The position of the aligned geometries after repeated co-registrations differed by few millimetres (median absolute shift along X, Y and Z axes was equal to 2.6, 2.9 and 2.3 mm, respectively) and degrees (median absolute rotation about X, Y and Z axes was equal to 4.7, 3.1, 13.3° respectively) (Supplementary Table 3). Pair-wise correlation coefficients between AUC obtained using reference and additional co-registrations ranged between 0.83 and 0.88, while intraclass correlation coefficients measuring the agreement between AUC estimates across all configurations was equal to 0.86 and 0.88 for localization of  $V < 1.5$  mV and  $V < 0.5$  mV, respectively (Fig. S5 in Supplementary Material).

### Effect of spatial smoothing

Spatial smoothing gradually improved agreement between voltage and PSI maps. Maximum smoothing ( $R=6$  mm) in both PSI and voltage resulted in an increase in median PSI-voltage correlation coefficient of 13.7% ( $P=0.002$ , Figure 3C) and in median AUC of 5.8 ( $P=0.004$ , Figure 3C) with respect to non-smoothed maps. Effect of spatial smoothing applied in isolation or in combination to PSI and voltage maps is described in detail in the Supplementary Material (Fig. S6).

## Discussion

The aim of this study was to assess performance and limitations of low-voltage zones (LVZ) localisation by optimised LGE-CMR scar imaging in patients with CIEDs and co-registration algorithms for the delineation of scar in patients with CIEDs. We applied state of the art CMR imaging and electro-anatomical mapping to quantify spatial correlation between EAM voltage and PSI across all cardiac sites, focussing on the impact of co-registration and spatial resolution.



264 The main findings are: (1) PSI showed a significant inverse correlation with EAM  
265 voltage ( $r=-0.57$ , interquartile range -0.68, -0.42) and allowed localization of low-  
266 voltage zones with median sensitivity and specificity of 74% and 78%, (2) Small  
267 variations in EAM-CMR anatomical co-registration can worsen the localization of  
268 low-voltage zones, but the use of the ascending and descending aorta to guide co-  
269 registration ensures high intra- and inter-operator reproducibility.

270 With increasing numbers of patients with CIEDs considered for VT ablation due to  
271 recurrent arrhythmias and appropriate shocks, techniques are required to improve  
272 procedural success rates whilst reducing radiation dose and procedural times. LGE-  
273 CMR can aid scar localization and pre-procedural planning (2–7,16), however CMR  
274 in patients with CIEDs has generally been avoided due to concerns related to risk  
275 and poor image quality from device-related artefact. Few studies had previously  
276 investigated EAM and CMR in patients with CIEDs. These had focused on scar size  
277 (13), feasibility (17) and correlation between critical sites for re-entry initiation (8),  
278 but localization of low-voltage zones by CMR, which is crucial for VT catheter  
279 ablation, is still undetermined. This study provides the first assessment of the  
280 agreement between voltage and PSI maps in patients with CIEDs. Importantly, it  
281 provides quantitative assessment of the impact of co-registration misalignments,  
282 which has significant implications particularly in the context of a purely anatomical  
283 scar mapping strategy to identify corridors that support re-entry (8,9). Indeed, a  
284 recent study has shown that CMR-guided catheter ablation based on localization of  
285 critical sites of VT through advance image processing of PSI maps can reduce  
286 procedural time and improve outcomes of VT catheter ablation (9). Another potential  
287 application for CMR may be in combination with other non-invasive modalities to  
288 identify ablation target for stereotactic body radiotherapy (18,19). For instance, ECG-

Imaging could be used for identification of VT sites of origin and delineation of the functional electrophysiological substrate related to activation and repolarization abnormalities (14,15,20), whereas CMR could be used for scar delineation and identification of corridors supporting the VT circuit.

### Impact of EAM-CMR co-registration

Co-registration usually involves minimization of the distance between landmark points, followed by manual adjustment by expert operators. This can introduce bias, particularly if only LV models are used for alignment. We assessed the impact of small random alterations in the co-registration by algorithmically applying rotations and shifts to the EAM after co-registration. We found that these had an impact and that in some cases even small rotations and shifts considerably reduced the agreement between voltage and PSI maps. Despite this, we found that intra and inter-operator co-registration variability was low, and reproducibility of low-voltage zones localization was high (intraclass correlation of AUC equal to 0.86). This is the first study to assess the reproducibility of co-registration, which in this study was optimised by the utilization of the full 3D geometry of the ascending, arch, and descending aorta. The use of the full aortic geometry to co-register CMR and electro-anatomical data was proposed in one of the seminal studies on EAM-CMR integration (21) but has not been adopted as standard clinical practice. Previous studies have used other anatomical landmarks for co-registration, including the position of the mitral annulus, proximal aorta, pulmonary artery, RV or the ostium of the left main coronary artery (4,9) and one study has analysed the effects of rotation (but not shifts) on co-registration accuracy (22).

## 312 Methodological considerations

313 LGE-CMR correlates well histologically with various models of myocardial fibrosis  
314 (23) , but quantitative evaluation of LGE is challenging, with signal thresholding  
315 impacting on the projected infarct size. Despite good correlation between EAM  
316 voltage and PSI using fixed thresholds based on the median values across the  
317 cohort, the optimal PSI threshold varied considerably across cases, and there was a  
318 narrow gap between optimum thresholds for localization of low-voltage zones with  
319  $V < 1.5$  mV and  $V < 0.5$  mV. This highlights the challenge of delineating scar border-  
320 zones (0.5 – 1.5 mV), which beyond the limitations of spatial resolution inherent to  
321 each modality may be related to the effect of wall thickness (24), catheter  
322 configuration (25) , variable CMR contrast kinetics or residual hypersensitivity and  
323 signal void related to the presence of the ICD.

324 In primary analysis, we have reported averaged values across CMR layers spanning  
325 from sub-endocardium (layer 10%) to mid-myocardium (layer 50%). Layer-by-layer  
326 analysis has shown that localization of endocardial low-voltage zones was more  
327 accurate when using endocardial layers as compared to epicardial ones  
328 (Supplementary Figure S4). However, accuracy in low-voltage zones localization  
329 was not significantly different in the sub-endocardial PSI layers as compared to mid-  
330 myocardial ones. There are several possible explanations for this, predominantly  
331 driven by the limitations of the respective techniques. Whilst mid-myocardial scar  
332 may be less apparent on endocardial EAM, there are also challenges in segmenting  
333 the true endocardium with CMR and accurately demonstrating the blood-myocardial  
334 boundary. The proximity of the 10% layer to the blood pool may occasionally result in  
335 partial volume effects within the endocardial voxel which might introduce artefact in  
336 the reconstructed 3D model. Despite attempts to limit this by using thin 2D slices

(4mm), in some cases this cannot be corrected. This limitation is further accentuated in cases of severe ischaemic cardiomyopathy in view of the reduced wall thickness of infarcted myocardium.

Correlation between endocardial unipolar voltage and PSI was similar across all PSI layers, including deeper mid-myocardial and sub-epicardial layer (Supplementary Figure S3). Although endocardial unipolar voltage has been shown to enable localization of epicardial scar, evidence is stronger for non-ischaemic cardiomyopathy and in absence of endocardial scar (26). Furthermore, theoretical (27) and experimental (28) studies have demonstrated that the amplitude of the unipolar electrogram is mainly determined by remote activity (and in particular by the sequence of electrical depolarization) and therefore it is not an ideal parameter for localization of scar.

In this study, we used spatial smoothing to reduce noise in both voltage and PSI maps. Spatial smoothing improved agreement between voltage and PSI maps with moderate but significant increase in voltage-PSI correlation and low-voltage zone discrimination. However, since smoothing reduces spatial resolution, its use may be limited to the localization of large areas of scar as opposed to the fine details of the scar architecture.

## Limitations

Our study is limited by the small sample size. However, patients had high-density EAM and complete geometry of the aorta, which is crucial to ensure detailed delineation of the substrate and optimal co-registration. EAM was used as a reference for the identification of abnormal tissue, and although Pentaray was used to collect most points, an ablation catheter was occasionally used. Bipolar voltage

can be affected by wave-front directionality and catheter configuration (25). Although higher spatial resolution LGE imaging can be obtained using 3D MRI (1.9×1.9×1.9 mm<sup>3</sup>), 3D wideband LGE imaging is generally unfeasible in patients with frequent ventricular arrhythmias awaiting ablation. Finally, this study was limited to endocardial maps and did not focus on the utility of integrating CMR with EAM data during catheter ablations (6–8). This however should be the focus of further investigation.

## Conclusions

In patients with CIEDs, use of novel wideband CMR LGE sequences and strategies to optimize co-registration can localize areas of scar with good accuracy. To fully establish the role of CMR in assisting VT ablation, effort should be focused on standardising co-registration, improving data acquisition and reducing noise in both modalities.

## Perspectives

*Competency in medical knowledge:* This study shows that optimised cardiac MRI enables non-invasive localization of scar in patients with cardiac implantable electronic devices and it highlights the importance of using the thoracic aorta as a landmark for accurate co-registration with electro-anatomical maps.

*Translational outlook:* Optimised MRI sequences and accurate co-registration of cardiac MRI scar maps with electro-anatomical geometries could improve VT ablation.

## 384    **References**

- 385    1.    Graham AJ., Orini M., Lambiase PD. Limitations and challenges in mapping  
386        ventricular tachycardia: New technologies and future directions. *Arrhythmia*  
387        *Electrophysiol Rev* 2017;6(3):118–24. Doi: 10.15420/aer.2017.20.1.
- 388    2.    Ashikaga H., Sasano T., Dong J., et al. Magnetic resonance-based anatomical  
389        analysis of scar-related ventricular tachycardia: Implications for catheter  
390        ablation.        *Circ        Res        2007;101(9):939–47.        Doi:*  
391        10.1161/CIRCRESAHA.107.158980.
- 392    3.    Codreanu A., Odille F., Aliot E., et al. Electroanatomic Characterization of  
393        Post-Infarct Scars: Comparison With 3-Dimensional Myocardial Scar  
394        Reconstruction Based on Magnetic Resonance Imaging. *J Am Coll Cardiol*  
395        2008;52(10):839–42. Doi: 10.1016/J.JACC.2008.05.038.
- 396    4.    Wijnmaalen AP., Van Der Geest RJ., Van Huls Van Taxis CFB., et al. Head-to-  
397        head comparison of contrast-enhanced magnetic resonance imaging and  
398        electroanatomical voltage mapping to assess post-infarct scar characteristics  
399        in patients with ventricular tachycardias: Real-time image integration and  
400        reversed registration. *Eur Heart J* 2011;32(1):104–14. Doi:  
401        10.1093/eurheartj/ehq345.
- 402    5.    Sramko M., Hoogendoorn JC., Glashan CA., Zeppenfeld K. Advancement in  
403        cardiac imaging for treatment of ventricular arrhythmias in structural heart  
404        disease. *Europace* 2019;21(3):383–403. Doi: 10.1093/europace/euy150.
- 405    6.    Andreu D., Berruezo A., Ortiz-Pérez JT., et al. Integration of 3D  
406        electroanatomic maps and magnetic resonance scar characterization into the  
407        navigation system to guide ventricular tachycardia ablation. *Circ Arrhythmia*

- 408 Electrophysiol 2011;4(5):674–83. Doi: 10.1161/CIRCEP.111.961946.
- 409 7. Andreu D., Penela D., Acosta J., et al. Cardiac magnetic resonance–aided  
410 scar dechanneling: Influence on acute and long-term outcomes. Heart Rhythm  
411 2017;14(8):1121–8. Doi: 10.1016/j.hrthm.2017.05.018.
- 412 8. Roca-Luque I., Van Breukelen A., Alarcon F., et al. Ventricular scar channel  
413 entrances identified by new wideband cardiac magnetic resonance sequence  
414 to guide ventricular tachycardia ablation in patients with cardiac defibrillators.  
415 Europace 2020;22(4):598–606. Doi: 10.1093/europace/euaa021.
- 416 9. Soto-Iglesias D., Penela D., Jáuregui B., et al. Cardiac Magnetic Resonance-  
417 Guided Ventricular Tachycardia Substrate Ablation. JACC Clin Electrophysiol  
418 2020;6(4):436–47. Doi: 10.1016/j.jacep.2019.11.004.
- 419 10. Bhuva AN., Kellman P., Graham A., et al. Clinical impact of cardiovascular  
420 magnetic resonance with optimized myocardial scar detection in patients with  
421 cardiac implantable devices. Int J Cardiol 2019;279:72–8. Doi:  
422 10.1016/j.ijcard.2019.01.005.
- 423 11. Seewöster T., Löbe S., Hilbert S., et al. Cardiovascular magnetic resonance  
424 imaging in patients with cardiac implantable electronic devices: best practice  
425 and real-world experience. Europace 2019;21(8):1220–8. Doi:  
426 10.1093/europace/euz112.
- 427 12. Dickfeld T., Tian J., Ahmad G., et al. MRI-guided ventricular tachycardia  
428 ablation integration of late gadolinium-enhanced 3D scar in patients with  
429 implantable cardioverter- defibrillators. Circ Arrhythmia Electrophysiol  
430 2011;4(2):172–84. Doi: 10.1161/CIRCEP.110.958744.

- 431 13. Stevens SM., Tung R., Rashid S., et al. Device artifact reduction for magnetic  
432 resonance imaging of patients with implantable cardioverter-defibrillators and  
433 ventricular tachycardia: Late gadolinium enhancement correlation with  
434 electroanatomic mapping. *Heart Rhythm* 2014;11(2):289–98. Doi:  
435 10.1016/j.hrthm.2013.10.032.
- 436 14. Graham AJ., Orini M., Zacur E., et al. Simultaneous Comparison of  
437 Electrocardiographic Imaging and Epicardial Contact Mapping in Structural  
438 Heart Disease. *Circ Arrhythmia Electrophysiol* 2019;12(4):e007120. Doi:  
439 10.1161/CIRCEP.118.007120.
- 440 15. Graham AJ., Orini M., Zacur E., et al. Evaluation of ECG Imaging to Map  
441 Haemodynamically Stable and Unstable Ventricular Arrhythmias. *Circ*  
442 *Arrhythmia Electrophysiol* 2020. Doi: 10.1161/circep.119.007377.
- 443 16. Desjardins B., Crawford T., Good E., et al. Infarct architecture and  
444 characteristics on delayed enhanced magnetic resonance imaging and  
445 electroanatomic mapping in patients with postinfarction ventricular arrhythmia.  
446 *Heart Rhythm* 2009;6(5):644–51. Doi: 10.1016/j.hrthm.2009.02.018.
- 447 17. Singh A., Kawaji K., Goyal N., et al. Feasibility of Cardiac Magnetic Resonance  
448 Wideband Protocol in Patients With Implantable Cardioverter Defibrillators and  
449 Its Utility for Defining Scar. *Am J Cardiol* 2019;123(8):1329–35. Doi:  
450 10.1016/j.amjcard.2019.01.018.
- 451 18. Robinson CG., Samson PP., Moore KMS., et al. Phase I/II Trial of  
452 Electrophysiology-Guided Noninvasive Cardiac Radioablation for Ventricular  
453 Tachycardia. *Circulation* 2019;139(3):313–21. Doi:  
454 10.1161/CIRCULATIONAHA.118.038261.



- 455 19. Cuculich PS., Schill MR., Kashani R., et al. Noninvasive Cardiac Radiation for  
456 Ablation of Ventricular Tachycardia. *N Engl J Med* 2017;377(24):2325–36. Doi:  
457 10.1056/nejmoa1613773.
- 458 20. Wang Y., Cuculich PS., Zhang J., et al. Noninvasive Electroanatomic Mapping  
459 of Human Ventricular Arrhythmias with Electrocardiographic Imaging. *Sci*  
460 *Transl Med* 2011;3(98):98ra84-98ra84. Doi: 10.1126/scitranslmed.3002152.
- 461 21. Reddy VY., Malchano ZJ., Holmvang G., et al. Integration of cardiac magnetic  
462 resonance imaging with three-dimensional electroanatomic mapping to guide  
463 left ventricular catheter manipulation: Feasibility in a porcine model of healed  
464 myocardial infarction. *J Am Coll Cardiol* 2004;44(11):2202–13. Doi:  
465 10.1016/j.jacc.2004.08.063.
- 466 22. Tao Q., Milles J., Van Huls Van Taxis C., et al. Toward magnetic resonance-  
467 guided electroanatomical voltage mapping for catheter ablation of scar-related  
468 ventricular tachycardia: A comparison of registration methods. *J Cardiovasc*  
469 *Electrophysiol* 2012;23(1):74–80. Doi: 10.1111/j.1540-8167.2011.02167.x.
- 470 23. Iles LM., Ellims AH., Llewellyn H., et al. Histological validation of cardiac  
471 magnetic resonance analysis of regional and diffuse interstitial myocardial  
472 fibrosis. *Eur Heart J Cardiovasc Imaging* 2015;16(1):14–22. Doi:  
473 10.1093/ehjci/jeu182.
- 474 24. Glashan CA., Androulakis AFA., Tao Q., et al. Whole human heart histology to  
475 validate electroanatomical voltage mapping in patients with non-ischaemic  
476 cardiomyopathy and ventricular tachycardia. *Eur Heart J* 2018;39(31):2867–  
477 75. Doi: 10.1093/eurheartj/ehy168.
- 478 25. Takigawa M., Relan J., Kitamura T., et al. Impact of Spacing and Orientation

on the Scar Threshold With a High-Density Grid Catheter. *Circ Arrhythmia Electrophysiol* 2019;12(9):e007158. Doi: 10.1161/CIRCEP.119.007158.

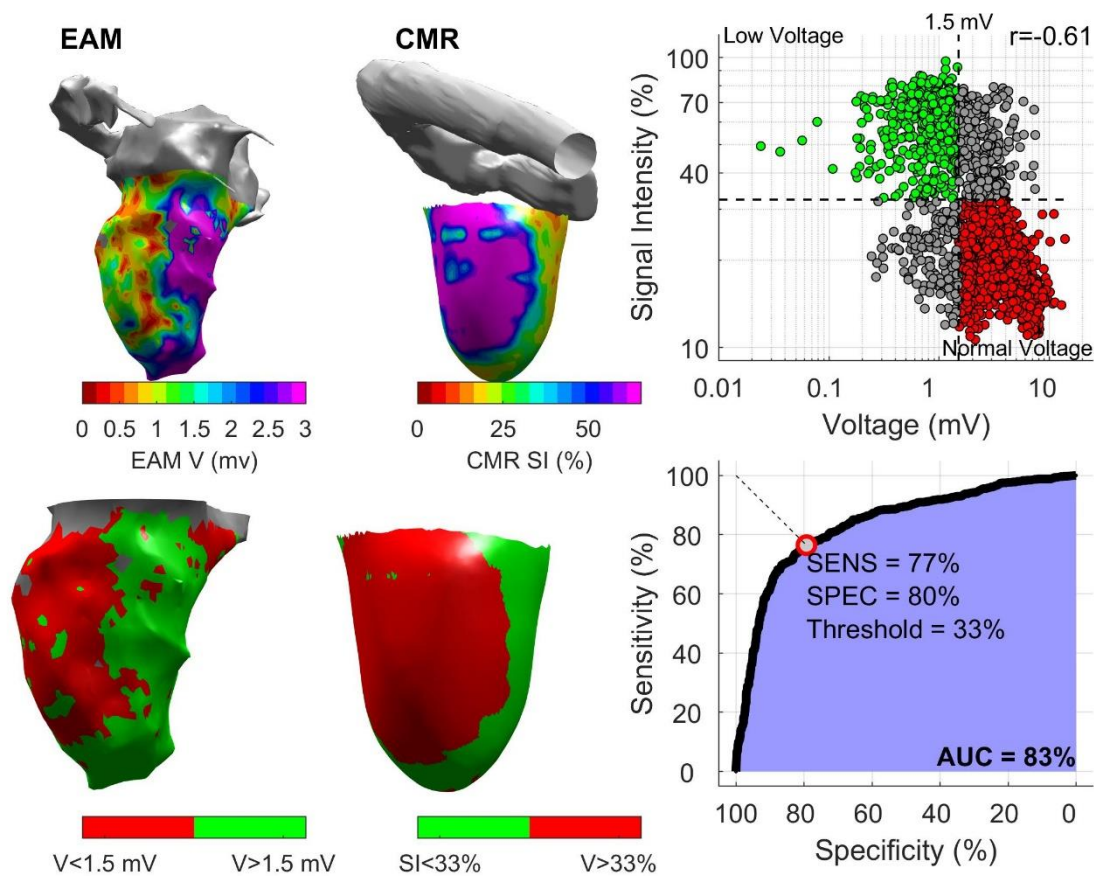
26. Hutchinson MD., Gerstenfeld EP., Desjardins B., et al. Endocardial unipolar voltage mapping to detect epicardial ventricular tachycardia substrate in patients with nonischemic left ventricular cardiomyopathy. *Circ Arrhythmia Electrophysiol* 2011;4(1):49–55. Doi: 10.1161/CIRCEP.110.959957.

27. Potse M., Vinet A., Opthof T., Coronel R. Validation of a simple model for the morphology of the T wave in unipolar electrograms. *Am J Physiol Heart Circ Physiol* 2009;297(2):H792–801. Doi: 10.1152/ajpheart.00064.2009.

28. Orini M., Taggart P., Lambiase PD. In vivo human sock-mapping validation of a simple model that explains unipolar electrogram morphology in relation to conduction-repolarization dynamics. *J Cardiovasc Electrophysiol* 2018;29(7):990–7. Doi: 10.1111/jce.13606.

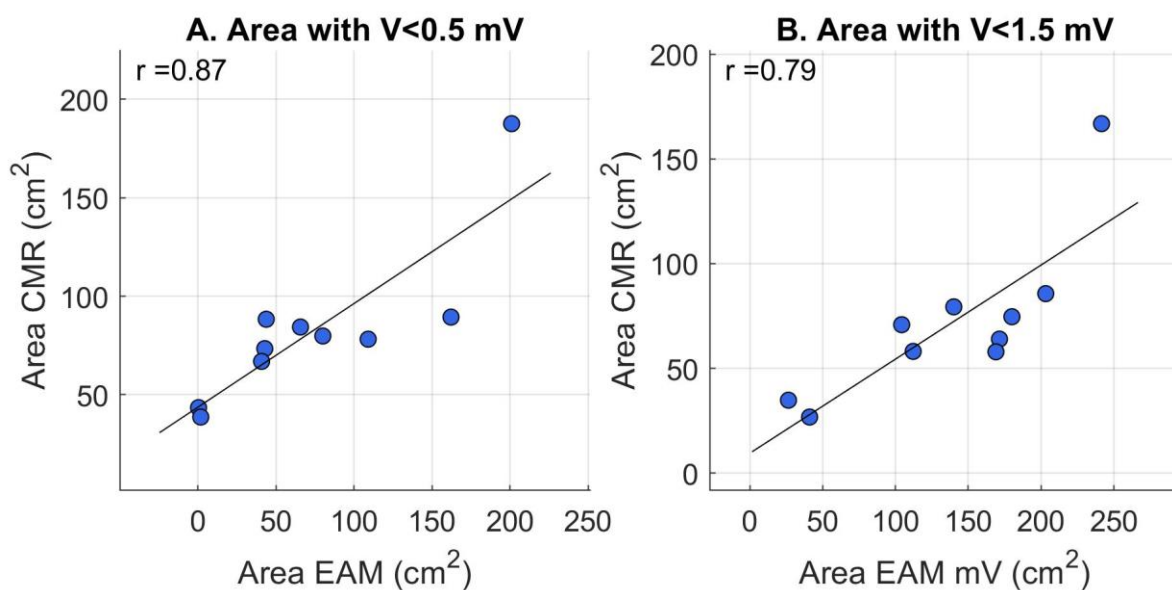
## Figures

Figure 1.



**Figure 1:** Comparison between EAM and LGE-CMR (example Subject #9). Top: voltage and CMR-intensity maps (30 transmural) shown side-by-side. Bottom: Low-voltage areas ( $V < 1.5$  mV) and areas with  $PSI > 33\%$  indicating abnormal tissue are shown on the left and right, respectively. Maps from left to right are shown in the same reference system. Top-right inset shows correlation between voltage and PSI (on loglog scale), with green representing true positives and red representing true negative. Correlation coefficient was  $r = -0.61$ . Bottom-right inset shows ROC curve with a circle representing optimal threshold for identification of low-voltage zones. EAM: Electroanatomical map. LGE-CMR: Late gadolinium enhancement cardiovascular magnetic resonance. AUC: Area under the ROC curve.

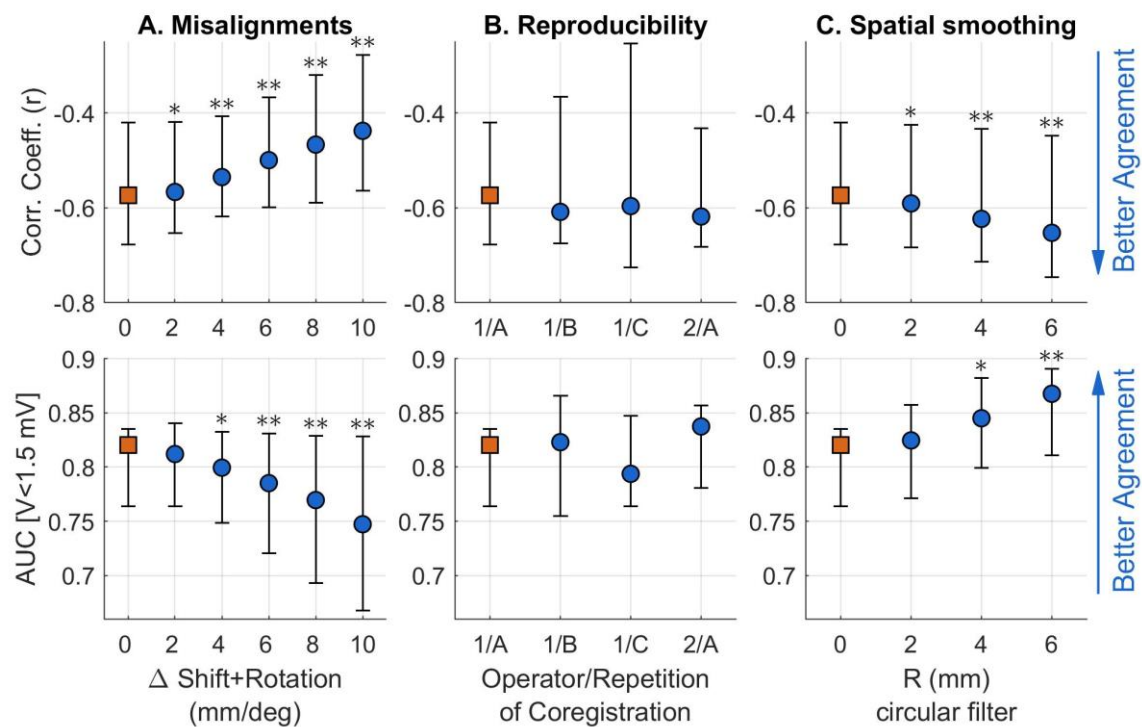
507 Figure 2.



508

509 **Figure 2:** Correlation across all subjects between scar area measured using EAM  
510 and CMR-LGE automated scar segmentation. Linear fitting is reported with a solid  
511 line and correlation coefficient ( $r$ ) is shown on the top-left corner. On EAM, low-  
512 voltage zones were defined with  $V < 0.5$  mV and  $V < 1.5$  mV. On CMR maps, areas  
513 representing low-voltage zones were identified with case-specific thresholds  
514 obtained through ROC analysis (average of layers spanning from sub-endocardium,  
515 layer 10, to mid-myocardium, layer 50).

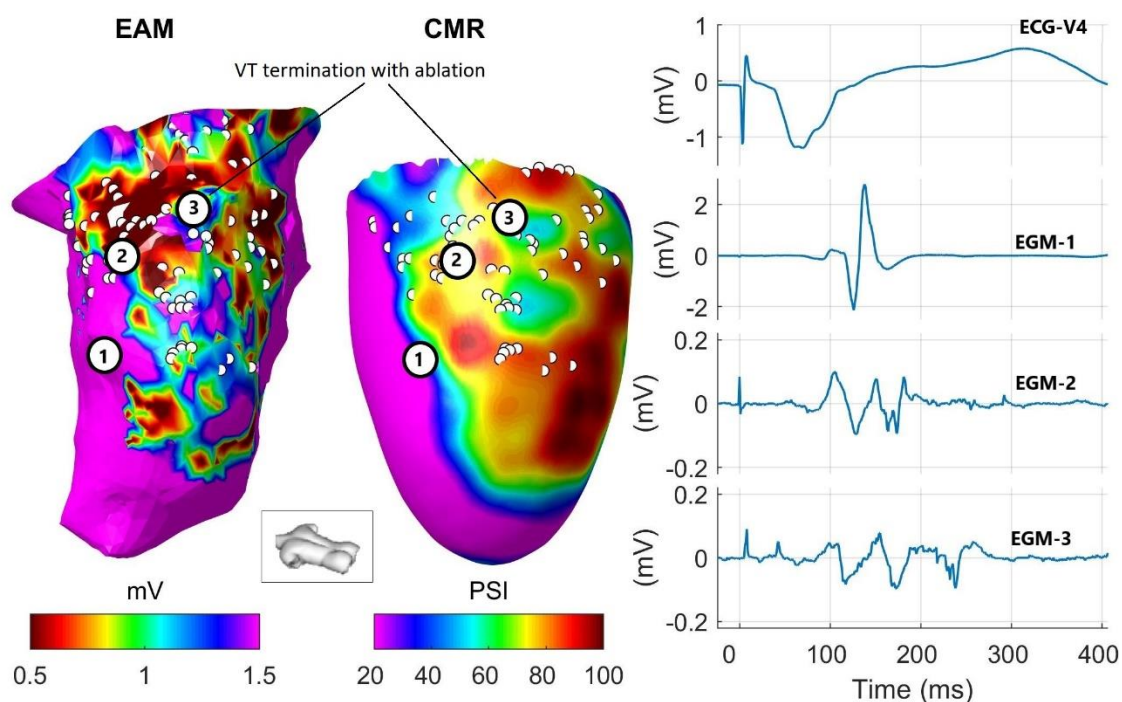
516 **Figure 3.**



517

518 **Figure 3:** Effect of misalignment in co-registration (A), inter- and intra-operator  
519 variability of co-registration (B) and spatial smoothing of voltage and pixel intensity  
520 signal (PSI) maps (C) on EAM-CMR agreement. A: Expert-based co-registration of  
521 each case was algorithmically modified by simultaneously shifting ( $\Delta$  mm) and  
522 rotating ( $\Delta$  deg) the voltage map along and across the 3 orthogonal axes (64 iteration  
523 per  $\Delta$  and patient). B: EAM and voltage maps were co-registered by a first operator  
524 three times (1A, 1B and 1C) and by a second operator (2A). C: Increasing degree of  
525 spatial smoothing of voltage and PSI maps using a circular filter of radius equal to 2,  
526 4 and 6 mm. Markers and whiskers represent median value and interquartile range.  
527 r: Spearman's correlation coefficient between PSI and voltage across cardiac sites.  
528 AUC: Area under the ROC curve for localization of zones with  $V<1.5$  mV. \*  $P<0.05$ ;  
529 \*\*  $P<0.005$  (Wilcoxon signed-rank test) with respect to reference values (red  
530 squares, corresponding to  $\Delta=0$  in A; 1A in B;  $R=0$  in C).

531 **Figure 4**



533 **Figure 4:** Left: Electro-anatomical map (EAM) collected while pacing from the RV  
 534 apex and CMR pixel signal intensity (PSI) map (endocardial layer corresponding to  
 535 10% of wall thickness). White dots indicate ablation sites projected onto the two  
 536 geometries. Electrograms (EGM) from sites labelled 1 (healthy tissue), 2 (dense  
 537 scar) and 3 (VT exit site) are shown on the right as EGM-1,2 and 3. Ablation  
 538 proximal to site 3 terminated ventricular tachycardia induced after substrate  
 539 mapping. Note y-scale is adjusted to the signal's amplitude.

540

541 **Tables**

542 **Table 1**

ID	Sex (M/F)	Age (years)	Aetiology	Type of Device	MR Conditional	LVEF (%)	Artefacts (% of myocardium)	Interval CMR-ablation (weeks)	First/ Redo Ablation
1	M	68	IHD	CRTD	No	52	13.9	0.3	First
2	M	69	IHD	ICD	Yes	34	1.4	44.3	First
3	M	79	IHD	CRTD	No	16	0.0	0.9	Redo
4	M	84	IHD	ICD	No	19	9.7	4.0	First
5	F	79	IHD	ICD	Yes	20	9.8	0.6	First
6	M	84	IHD	ICD	No	25	10.2	0.0	First
7	M	78	IHD	CRTD	Yes	10	8.8	0.0	Redo
8	M	56	DCM	CRTD	No	20	28.9	0.3	First
9	M	73	IHD	ICD	Yes	41	0.2	8.3	First
10	M	72	IHD	CRTD	Yes	23	25.9	1.0	First

543

544 **Table 1: Baseline demographics, clinical and CMR data of the patient cohort.**

545 CMR-EP interval: time delay between CMR and VT ablation.

546

547 **Table 2**

Patient number	Points		Corr. Coeff.	V<0.5 mV					V<1.5 mV				
	EAM Mesh	Paired (%)		PREV (%)	AUC	THR (%)	SENS (%)	SPEC (%)	PREV (%)	AUC (%)	THR (%)	SENS (%)	SPEC (%)
1	3,871	58	-0.54	1	-	-	-	-	22	0.76	50	74	71
2	22,669	83	-0.32	22	0.58	35	64	54	55	0.70	33	68	67
3	7,947	48	-0.68	35	0.87	46	83	77	63	0.83	42	73	79
4	7,770	43	-0.69	22	0.83	50	83	72	62	0.87	41	78	83
5	6,880	65	-0.42	30	0.77	51	80	72	56	0.69	47	64	73
6	14,952	55	-0.50	49	0.80	41	72	76	76	0.81	37	71	78
7	15,583	41	-0.73	54	0.91	53	85	87	72	0.87	46	76	86
8	8,896	61	-0.61	22	0.79	49	78	69	44	0.83	44	80	76
9	2,438	88	-0.61	5	0.75	38	81	66	36	0.83	33	77	80
10	7,674	60	-0.31	80	0.69	36	77	60	96	0.79	33	75	84
<b>Median</b>	<b>7,859</b>	<b>59</b>	<b>-0.57</b>	<b>26</b>	<b>0.79</b>	<b>46</b>	<b>80</b>	<b>72</b>	<b>59</b>	<b>0.82</b>	<b>41</b>	<b>74</b>	<b>78</b>
Q1	6,880	48	-0.68	22	0.73	37	76	65	44	0.76	33	71	73
Q3	14,952	65	-0.42	49	0.84	51	83	76	72	0.83	46	77	83

548

549 **Table 2:** Low-voltage zone localization. EAM: Electroanatomical map. MED: Median.

550 Q1 and Q3: First and third quartile, respectively. PREV: Prevalence of LVZ across

551 paired points. AUC: Area under the ROC curve. THR: PSI Case-specific threshold.

552 SENS: Sensitivity. SPEC: Specificity.